A&A 583, A117 (2015)
DOI: 10.1051/0004-6361/201526436

Astronomy & Astrophysics

New *XMM-Newton* observation of the thermally emitting isolated neutron star 2XMM J104608.7-594306⋆

A. M. Pires[1], C. Motch[2], R. Turolla[3,4], S. B. Popov[5], A. D. Schwope[1], and A. Treves[6]

[1] Leibniz-Institut für Astrophysik Potsdam (AIP), An der Sternwarte 16, 14482 Potsdam, Germany
e-mail: apires@aip.de
[2] Observatoire Astronomique de Strasbourg, Université de Strasbourg, CNRS, UMR 7550, 11 rue de l'Université, 67000 Strasbourg, France
[3] Universitá di Padova, Dipartimento di Fisica e Astronomia, via Marzolo 8, 35131 Padova, Italy
[4] Mullard Space Science Laboratory, University College London, Holmbury St. Mary, Dorking, Surrey, RH5 6NT, UK
[5] Sternberg Astronomical Institute, Lomonosov Moscow State University, Universitetskii pr. 13, 119991 Moscow, Russia
[6] Universitá dell'Insubria, Dipartimento di Fisica e Matematica, via Valleggio 11, 22100 Como, Italy

Received 29 April 2015 / Accepted 20 August 2015

ABSTRACT

Context. The isolated neutron star (INS) 2XMM J104608.7-594306 is one of the only two to be discovered through their thermal emission since the ROSAT era. Possibly a remnant of a former generation of massive stars in the Carina nebula, the exact nature of the source is unclear, and it might be unique amongst the several classes of Galactic INSs.
Aims. In a first dedicated *XMM-Newton* observation of the source, we found intriguing evidence of a very fast spin period of $P \sim 18.6$ ms at the 4σ confidence level. Moreover, spectral features in absorption have also been identified. We re-observed 2XMM J104608.7-594306 with *XMM-Newton* to better characterise the spectral energy distribution of the source, confirm the candidate spin period, and possibly constrain the pulsar spin-down.
Methods. We used the two *XMM-Newton* observations of 2XMM J104608.7-594306 to perform detailed timing and spectral X-ray analysis. Both the spin-down rate and the energy of the spectral features provide estimates on the neutron star magnetic field, which are crucial for investigating the evolutionary state of the neutron star.
Results. Statistically acceptable spectral fits and meaningful physical parameters for the source are only obtained when the residuals at energies 0.55 keV and 1.35 keV are taken into account by the spectral modelling. While the former can result from the inhomogeneous temperature distribution on the surface of the neutron star or can be related to a local overabundance of oxygen in the Carina nebula, the one at 1.35 keV is only satisfactorily accounted for by invoking a line in absorption. In this case, the best-fit neutron star atmosphere models constrain the hydrogen column density, the effective temperature, and the luminosity of the source within $N_{\rm H} = (2.5{-}3.3) \times 10^{21}$ cm^{-2}, $T_{\rm eff} = (6{-}10) \times 10^5$ K, and $L_{\rm X} = (1.1{-}7.4) \times 10^{32}$ erg s^{-1}. The implied distance is consistent with a location in (or in front of) the Carina nebula, and radiation radii are compatible with emission originating on most of the surface. Non-thermal X-ray emission is ruled out at levels above 0.5% (3σ) of the source luminosity. Unfortunately, the second *XMM-Newton* observation proved inconclusive in terms of confirming (discarding) the fast candidate spin, providing an upper limit on the pulsed fraction of the source that is very close to the limiting sensitivity for detecting the modulation found previously.
Conclusions. In the absence of an unambiguous period determination and an estimate of the magnetic field, the nature of the source remains open to interpretation. Its likely association with the Carina cluster and its overall spectral properties (only shared by a handful of other peculiar INSs) disfavour a standard evolutionary path or one in which the source was previously recycled by accretion in a binary system. The star 2XMM J104608.7-594306 may be similar to Calvera (1RXS J141256.0+792204), a neutron star for which the scenario of an evolved anti-magnetar has been discussed. A better age estimate and deeper radio and γ-ray limits are required to further constrain the evolutionary state of the neutron star.

Key words. stars: neutron – pulsars: general – X-rays: individuals: 2XMM J104608.7-594306

1. Introduction

In the standard scenario of pulsar evolution, a neutron star is born rotating fast. As a consequence of rotational energy losses, it is expected to evolve towards longer periods until electron-positron pairs can no longer be produced; the radio emission ceases and the pulsar crosses the so-called death line. The radio emission is, however, energetically unimportant relative to the power emitted at high energies. While young, these objects are strong sources of X-ray and γ-ray emission with radiative processes that include non-thermal emission from charged particles that were accelerated in the pulsar magnetosphere and thermal emission from the hot surface. However, after a maximum of $\sim 10^7$ yr, pulsars have probably exhausted their internal source of particle creation and acceleration and cooled down to temperatures undetectable in X-rays.

This relatively simple picture has been challenged by the discovery of peculiar groups of isolated neutron stars (INSs) that are radio quiet or transient. Their (mostly unpredicted) properties significantly differ from those displayed by standard pulsars (see Kaspi 2010; Harding 2013, for an overview and references). Among them are magnetars (anomalous X-ray

⋆ Based on observations obtained with *XMM-Newton*, an ESA science mission with instruments and contributions directly funded by ESA Member States and NASA (Target 2XMM J104608.7-594306, obsids 0650840101, 0691970101).

pulsars (AXPs) and soft gamma repeaters (SGRs)), the central compact objects in supernova remnants (CCOs), the rotating radio transients (RRATs), and the ROSAT-discovered thermally-emitting INSs, also known as the Magnificent Seven (M7).

In particular, the M7 constitute a nearby ($d \lesssim 1$ kpc) group of middle-aged (0.1−1 Myr) neutron stars, observable through their bright and purely thermal X-ray emission (see, for example, Haberl 2007; Kaplan 2008; Turolla 2009, for reviews). Amounting to about half of all young INSs known in the solar neighbourhood (Popov et al. 2003), they could be as numerous as radio pulsars, with consequences for the total number of neutron stars populating the Milky Way (see Keane & Kramer 2008). Timing studies in X-rays (see Kaplan & van Kerkwijk 2011, and references therein) have shown that the M7 rotate more slowly ($P \sim 3$−11 s) and have higher magnetic field intensities, $B_{\rm dip} \sim (1-3) \times 10^{13}$ G, than the bulk of the (rotation-powered) radio pulsar population. Also at variance with pulsars detected at high energies, the X-ray luminosity of the M7 is in excess of the spin-down power. To a certain extent, such properties resemble those of the young and energetic magnetars (see, for example, Mereghetti 2008, for a review). On the other hand, the M7 experience less dramatic spin-down and do not show the complex phenomenology usually observed in magnetars (e.g. emission of flares, bursts, quasi-periodic oscillations, spectral variability, timing noise, etc.).

Another group consisting of radio-quiet, thermally emitting INSs, is that of CCOs (see, for example, de Luca 2008; Gotthelf & Halpern 2010; Halpern & Gotthelf 2010, for reviews). CCOs were first observed as point-like, radio-quiet X-ray sources, located near the geometrical centre of supernova remnants. Of the dozen objects known at present, including other candidates, at least three fit in the anti-magnetar scenario, in which these sources are young (aged 10^3 yr to 10^4 yr) and weakly magnetised ($B_{\rm dip} = 10^{10}$−10^{11} G) neutron stars that are experiencing very low spin-down (Gotthelf et al. 2013a, and references therein).

If the weak dipolar field of anti-magnetars remains constant, they are confined to a region of the $P - \dot{P}$ diagram of INSs that is devoid of other pulsars, between those occupied by the normal and millisecond (recycled) part of the population. The fact that no old (orphaned, or without a supernova remnant) CCO is recognised in this region of the $P - \dot{P}$ diagram in either radio or X-ray surveys (Halpern & Gotthelf 2010; Gotthelf et al. 2013b; Luo et al. 2015; see also Bogdanov et al. 2014, who searched for CCO descendants among supposedly old radio pulsars in supernova remnants) may favour the alternative scenario of field burial by hypercritical accretion (e.g. Chevalier 1989; Geppert et al. 1999; Viganò et al. 2012). In this scenario, the original neutron star magnetic field is submerged by fallback accretion of supernova ejecta, remaining hidden for several $\sim 10^3$ yr to 10^5 yr. As a result, the neutron star shows, in its early evolution, the typical anti-magnetar behaviour. As the field re-emerges, the pulsar quickly joins the rest of the population, moving upwards in the $P - \dot{P}$ diagram; its subsequent evolution would then follow according to the original field intensity. Residual thermal luminosity in the first $\sim 10^4$ yr, as well as enhanced cooling after $\sim 10^5$ yr, compared to its peers of similar characteristic ages, are expected to result from the accreted light-element envelope (e.g. Yakovlev & Pethick 2004).

For several years, considerable efforts have been made to discover new thermally emitting INSs (e.g. Chieregato et al. 2005; Turner et al. 2010; Agüeros et al. 2011). The INS 2XMM J104608.7-594306 (hereafter J1046), is one of only two to be discovered through their thermal emission and lack of obvious counterparts since the ROSAT era (Pires et al. 2009a). Possibly a remnant of a former generation of massive stars in the Carina nebula (Townsley et al. 2011), its exact nature is not clear, and it may be unique. The other source, 1RXS J141256.0+792204, also known as Calvera (Rutledge et al. 2008), is a relatively bright ROSAT source with a short spin period of $P \sim 59$ ms (Zane et al. 2011). Calvera is the only INS to date to be recognised as an evolved anti-magnetar, with a magnetic field of $B_{\rm dip} = 4.4 \times 10^{11}$ G that is, possibly, regaining its original strength (Halpern et al. 2013).

Thanks to its proximity (angular distance of 8.5′) to the well-studied Eta Carinae system, J1046 was serendipitously detected on many occasions by the *XMM-Newton* Observatory (Jansen et al. 2001). The analysis of the serendipitous data shows no significant long-term variability in either the X-ray flux or in the overall spectral properties of the source (Pires et al. 2009b). Follow-up observations in the optical with the European Southern Observatory Very Large Telescope (ESO-VLT) set a deep limit on the brightness of the optical counterpart, $m_{\rm V} > 27$ (2σ), and a very high X-ray-to-optical flux ratio of $\log(F_{\rm X}/F_{\rm V}) > 3.8$. At present, no radio or γ-ray counterparts are known.

As revealed by a first dedicated *XMM-Newton* observation, performed on 2010 December 6 (AO9, as reference for the text), the spectral energy distribution of J1046 is soft and purely thermal with significant deviations from a blackbody continuum of $kT \sim 135$ eV (Pires et al. 2012). While these properties are reminiscent of those of the middle-aged M7, the *XMM-Newton* observation also revealed intriguing evidence of a very fast rotation, at $P \sim 18.6$ ms. Such a rapid spin is difficult to reconcile with the spectral properties of the source.

We re-observed J1046 with *XMM-Newton* two years later to further improve the characterisation of the source's spectral energy distribution, confirm the candidate spin period, and eventually constrain the pulsar spin-down. We report here the results of this observation in detail. We also reanalysed the AO9 dataset to consistently compare our findings in a joined timing and spectral X-ray analysis. The paper's outline is as follows: in Sect. 2 we describe the new *XMM-Newton* observation and the data reduction. Analysis and results are presented in detail in Sect. 3. We examine the evolutionary state and possible nature of the neutron star in light of the observed properties of the known galactic INS population in Sect. 4. The main conclusions and results are summarised in Sect. 5.

Table 1. Instrumental configuration and duration of the EPIC scientific exposures of the *XMM-Newton* AO11 observation of 2XMM J104608.7-594306.

Instrument	Start time (UTC)	Mode	Duration (s)
pn	2012-12-20T19:45:17	SW	87 277
MOS1	2012-12-20T19:40:02	FF	87 532
MOS2	2012-12-20T19:40:02	FF	87 520

Notes. The EPIC cameras were operated in imaging mode and the thin filter was used (obsid 0691970101).

2. *XMM-Newton* observation and data reduction

For details on the instrumentation set-up and execution of the AO9 observation, we refer to Pires et al. (2012). The new *XMM-Newton* observation of J1046 (AO11) was carried out on 2012 December 20 for a total exposure time of 87.714 ks. Table 1

Table 2. Parameters of 2XMM J104608.7-594306, as extracted from the AO11 (and AO9) *XMM-Newton* EPIC images.

Parameter	pn	MOS1	MOS2	EPIC	EPIC (AO9)
Detection likelihood	6596	1613	2280	10 567	8952
Counts	$5.54(9) \times 10^3$	$1.55(5) \times 10^3$	$1.71(5) \times 10^3$	$8.85(12) \times 10^3$	$7.83(11) \times 10^3$
Counts (0.2−0.5 keV)	$1.11(4) \times 10^3$	$2.70(22) \times 10^2$	$2.25(18) \times 10^2$	$1.61(5) \times 10^3$	$1.53(5) \times 10^3$
Counts (0.5−1.0 keV	$3.50(7) \times 10^3$	$8.3(4) \times 10^2$	$1.00(3) \times 10^3$	$5.36(9) \times 10^3$	$4.73(9) \times 10^3$
Counts (1.0−2.0 keV)	$9.2(4) \times 10^2$	$4.44(29) \times 10^2$	$4.81(27) \times 10^2$	$1.86(5) \times 10^3$	$1.56(5) \times 10^3$
Counts (2.0−4.5 keV)	11 ± 11	0 ± 2.0	0.0 ± 2.0	13 ± 11	0 ± 4
Counts (4.5−12 keV)	2 ± 6	0 ± 2.0	4 ± 4	5 ± 7	12 ± 10
Rate (10^{-2} s^{-1})	9.18(15)	2.23(8)	2.18(6)	13.67(18)	13.27(19)
HR_1	0.518 ± 0.015	0.51 ± 0.03	0.633 ± 0.027	0.539 ± 0.012	0.511 ± 0.013
HR_2	-0.585 ± 0.015	-0.31 ± 0.04	-0.35 ± 0.03	-0.485 ± 0.012	-0.505 ± 0.014
HR_3	-0.976 ± 0.023	-1.000 ± 0.007	-1.000 ± 0.010	-0.986 ± 0.012	-1.000 ± 0.006
RA	10 46 08.75(15)	10 46 08.77(26)	10 46 08.76(21)	10 46 08.7(6)†	10 46 08.8(4)†
Dec	−59 43 05.32(15)	−59 43 04.97(26)	−59 43 05.07(21)	−59 43 06.7(5)†	−59 43 06.8(5)†

Notes. Counts and rates are given in the total *XMM-Newton* energy band (0.2−12 keV), unless otherwise specified. $^{(\dagger)}$ The marked EPIC source coordinates are astrometrically corrected, using as reference the 2MASS catalogue (see text). The corresponding 1σ errors take the astrometric errors into account.

contains information on the scientific exposures and instrumentation set-up of the EPIC pn (Strüder et al. 2001) and MOS (Turner et al. 2001) detectors. We adopted the thin filter for all EPIC instruments, given its better response at soft X-ray energies and the very low (<1%) expected level of spectral pile-up at aimpoint. The pn camera was operated in small window (SW) mode, providing high time resolution (6 ms) at the expense of a reduced exposure (deadtime of ∼29%). Although the MOS cameras operating in timing uncompressed mode could provide sufficient resolution (1.75 ms) for investigating the periodicity at $P \sim 18.6$ ms, calibration uncertainties between the EPIC detectors (e.g. Zane et al. 2011) and the impossibility of using the data for spectral analysis or for astrometrical corrections motivated us to choose the full-frame (FF) imaging mode instead. Standard data reduction was performed with SAS 13 (xmmsas_20131209_1901-13.5.0), using the latest calibration files. We processed the MOS and pn raw event files using the EPIC meta tasks emchain and epchain, respectively, applying default corrections. We ensured that the pn event file was clean of unrecognised time jumps (i.e. those uncorrected by standard SAS processing) by checking the output files of the epproc routine. Additionally, we reprocessed and reduced the AO9 observation consistent with the new dataset.

A few minor background flares were registered during the observation, effectively reducing the exposures in the MOS1 and MOS2 cameras to 79 ks and 84 ks, respectively. In the pn camera, the background level for the duration of the observation was below what is recommended by standard filtering of "good-time intervals". Therefore, the effective observing time (60 ks) was only reduced by the camera livetime in SW mode.

For the analysis, we filtered the event lists to exclude bad CCD pixels and columns, as well as to retain the predefined photon patterns with the highest quality energy calibration. Unless otherwise noted, single and double events were selected for pn (pattern ≤4) and single, double, triple, and quadruple for MOS (pattern ≤12). We defined the source centroid for each EPIC camera with the task eregionanalyse, which results at optimal radii of ∼20″ (0.3−2 keV). Background circular regions of size 60″ to 100″ (depending on the camera) were defined off-source on the same CCD as the target whenever possible.

The detected source count rates, hardness ratios, and other parameters based on a maximum likelihood PSF fitting are listed in Table 2. These are determined with the SAS task emldetect on images created for each camera and in each of the five predefined *XMM-Newton* energy bands. For comparison, we also list the source parameters as determined from the EPIC detection in the AO9 observation. The errors are nominal 1σ statistical uncertainties. There is no sign of variability in the source's overall properties; typically, J1046 displays a very soft energy distribution, with no counts above 2 keV, and count rates and hardness ratios are consistent within errors between the two *XMM-Newton* observations (see also Sect. 3.1).

We used the task eposcorr to refine the astrometry, by cross-correlating the list of EPIC X-ray source positions with those of near-infrared (2MASS, Skrutskie et al. 2006) objects lying within 15′ from J1046. Based on a number of 60 X-ray/infrared matches, we found a slight offset in right ascension, not significant within the astrometric errors, and an offset of $1.6'' \pm 0.5''$ in declination. We double-checked the offsets with eposcorr using other catalogues, in particular the *Chandra* Carina Cluster Project catalogue of X-ray sources (CCCP; Broos et al. 2011), the Guide Star Catalog (GSC 2.3.2; Lasker et al. 2008), and the Naval Observatory Merged Astrometric Dataset (NOMAD; Zacharias et al. 2004). The EPIC source position (Table 2), updated accordingly, was found to be consistent within errors with previous determinations. For consistency, we revised the source position in the AO9 observation also by cross-correlating the EPIC source list with the 2MASS catalogue. We found offsets of $-2.6'' \pm 0.4''$ in right ascension and $1.6'' \pm 0.5''$ in declination (46 matches). The updated source coordinates in the AO9 epoch are also listed in Table 2.

The statistics for the EPIC lightcurves (corrected for bad pixels, deadtime, exposure, as well as background counts, and binned into 875 s intervals) show the 3σ upper limits for the rms fractional variation of 0.12, 0.11 and 0.24 for pn, MOS1, and MOS2, respectively. On the basis of the same lightcurves, the reduced chi-square, assuming a constant flux, is 1.02 (pn, 99 d.o.f.), 0.97, and 0.71 (MOS1 and MOS2; 98 d.o.f.).

3. Analysis and results

3.1. Spectral analysis

The analysis of the EPIC data is based on source and background spectra extracted from regions as described in Sect. 2, together with the respective response matrices and ancillary files created

Table 3. Best-fit spectral parameters and count rates of 2XMM J104608.7-594306 per *XMM-Newton* observation and EPIC camera.

Ref.	MJD	$N_{\rm H}$ ($\times 10^{21}$ cm^{-2})			kT (eV)			Net count rate ($\times 10^{-2}$ s^{-1})		
	(days)	pn	MOS1	MOS2	pn	MOS1	MOS2	pn	MOS1	MOS2
AO9	55 536.531753	$2.79^{+0.24}_{-0.23}$	$3.7^{+0.8}_{-0.7}$	$3.8^{+0.7}_{-0.6}$	135(3)	128(8)	131(7)	7.39(12)	1.54(6)	1.66(6)
AO11	56 282.326597	$3.21^{+0.27}_{-0.26}$	$3.7^{+0.6}_{-0.5}$	4.3(5)	133^{+4}_{-3}	131(6)	125(5)	7.39(12)	1.63(5)	1.73(5)
Simultaneous (per camera)		2.98(18)	$3.7^{+0.5}_{-0.4}$	4.1(4)	134.2(2.4)	130(5)	127(4)	7.39(17)	1.58(8)	1.70(8)
Simultaneous (EPIC)			3.20(15)			133.1(1.9)			21.34(20)	
Combined			2.69(13)			136.7(1.8)			21.94(19)	

Notes. Errors are 1σ confidence levels. The model fitted to the data is a simple absorbed blackbody (tbabs∗bbody). Reduced χ^2_ν values are within 0.9 and 3.4, for 23 to 30 degrees of freedom (individual fits). Count rates in energy band 0.3−12 keV are subtracted for the background.

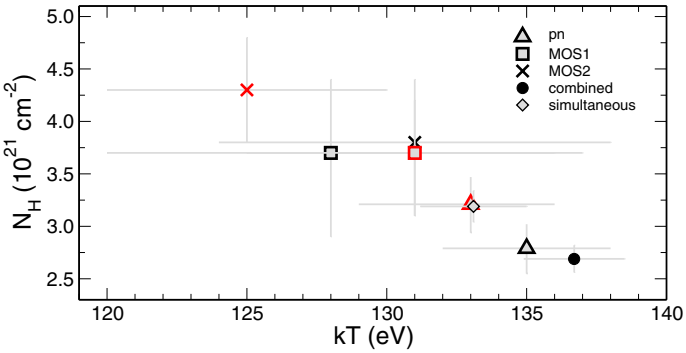

Fig. 1. Best-fit column density $N_{\rm H}$ as a function of blackbody temperature kT, for each individual (pn/MOS1/MOS2) spectrum used in the analysis (see legend). Also shown are the results by fitting all data simultaneously, as well as results of the stacked (combined) spectrum. AO11 datasets are highlighted in red. Error bars are 1σ confidence levels.

for each of the EPIC cameras. Owing to the frequent readout of pn in SW mode, detector noise dominates the low-energy count distribution. We therefore restricted the analysis of the pn camera to photons with energies above 0.35 keV. The energy band of the MOS cameras is restricted above 0.3 keV, which is in accordance with the guidelines and calibration status of the instrument. Including the AO9 observation, the available data amount to a total of six spectra and $\sim 1.7 \times 10^4$ counts (0.3−12 keV), of which 10% can be ascribed to background. For each spectrum, energy channels within 0.3/0.35 keV and 2 keV were rebinned according to a minimum number of 25 counts per spectral bin. We also took care not to oversample the instrument energy resolution at a given bin by more than a factor of three, which is especially important at low energies; this is done by fixing the parameter *oversample* = *3* in the SAS task specgroup.

To fit the spectra we used XSPEC 12.8.2 (Arnaud 1996). Unless otherwise noted, the fit parameters were allowed to vary freely and within reasonable ranges. The photoelectric absorption model and elemental abundances of Wilms et al. (2000, tbabs in XSPEC) were adopted to account for the interstellar absorption. Owing to the intrinsically soft energy distribution of J1046 and its location in the galactic plane ($b = -0.6°$), as well as to uncertainties resulting from the choice of abundance table in XSPEC, we estimate that the amount of intervening material derived from the spectral fits is uncertain by 15%.

First, we fitted each of the six spectra individually, using a simple absorbed blackbody model. The resulting best-fit parameters (Table 3 and Fig. 1) argue against any significant variability between the two *XMM-Newton* observations. However, the $N_{\rm H}$ and kT derived from the MOS spectra, even though statistically consistent, are systematically higher and softer, by 30% and 5% respectively, than those derived from pn. We then proceeded with the analysis using two different approaches, both relying on the assumption that the spectral parameters of J1046 are constant between the *XMM-Newton* observations: (i) we performed simultaneous fits of all spectra, where we allowed for a renormalisation factor to account for cross-calibration uncertainties between the detectors; and (ii) using the task epicspeccombine, we merged all six spectra and corresponding background and response files into one single, stacked dataset. While both approaches give a similarly well-constrained parameter space, the exercise shows that the best-fit $N_{\rm H}$ and kT, derived from the second approach, are biased and inconsistent with those from individual fits. On the other hand, the results from the first approach, while naturally dominated by the better statistics of the two pn spectra, are consistent with most measurements. We henceforth adopted for the spectral analysis simultaneous fits, including all EPIC data from the two *XMM-Newton* observations accordingly.

We summarise the results of the analysis in Tables 4–6. Table 4 contains the results of spectral fits where we assumed a (single- or double-temperature) blackbody continuum, and tested for different element abundances and for the presence of absorption lines. The fitted models are labelled (A) to (F), as reference for the text (see caption). To test for overabundance of elements with transitions in the range of 0.3 keV to 2 keV (C, N, O, Ne, Mg, etc.), we adopted the variable photoelectric absorption model vphabs and restricted abundance values in the range $1 < Z < 5$ in solar units.

The best-fit parameters of (more physically-motivated) neutron star atmosphere models are in Tables 5 and 6, where they are labelled (a) to (e). We tested magnetised and non-magnetised model atmospheres, consisting of fully- and partially-ionized hydrogen, as well as of carbon and other mid-Z elements (the models nsa, nsmaxg, and carbatm in XSPEC; see Zavlin et al. 1996; Pavlov et al. 1995; Ho et al. 2008; Mori & Ho 2007; Suleimanov et al. 2014). Wherever appropriate, the magnetic field was held fixed at values $B = 0, 10^{12}, 10^{13}$ G (nsa, Table 5); for nsmaxg, we tested 19 models with $B = (0.01-30) \times 10^{12}$ G (only the results with $\chi^2_\nu < 2$ are listed in Table 6). We first assumed canonical values for the neutron star mass and radius, $M_{\rm ns} = 1.4\,M_\odot$ and $R_{\rm ns} = 10$ km; these parameters were also allowed to vary to check for an improved fit. The size of the emission region, with respect to the neutron star physical radius, can also be parametrised for nsmaxg models; we restricted values to have $R_{\rm em} \leq R_{\rm ns}$. Finally, we also added a second thermal component, varied the elemental abundances, and added lines to the continuum to obtain statistically acceptable fits and derive plausible

Table 4. Results of spectral fitting of blackbody models.

Model	χ^2_ν (d.o.f.)	$N_{\rm H}$ ($\times 10^{21}$ cm^{-2})	kT_1^∞ (eV)	kT_2^∞ (eV)	ϵ_1 (keV)	ϵ_2 (keV)	$F_{\rm X}$ ‡ (erg s^{-1} cm^{-2})	R_1^∞ † (km)	R_2^∞ † (km)
(A)	1.98 (169)	3.20(15)	–	133.1(1.9)	–	–	$9.3^{+1.8}_{-1.5}\times10^{-13}$	–	$3.8^{+0.5}_{-0.4}$
(B)	1.34 (167)	5.3(3)	$28.6^{+2.3}_{-2.1}$	117.8(2.2)	–	–	$6^{+2.4}_{-3}\times10^{-10}$	$4^{+4}_{-2}\times10^{3a}$	$6.8^{+0.8}_{-0.7}$
(C)	1.48 (168)	3.75(17)	–	121.3(2.1)	–	–	$1.5^{+0.9}_{-0.5}\times10^{-12}$	–	$5.8^{+4}_{-2.2}$
(D)	1.08 (165)	$2.17^{+0.22}_{-0.20}$	–	157(5)	–	$1.289^{+0.018}_{-0.017}$	$4.6^{+6}_{-1.4}\times10^{-13}$	–	$1.9^{+5}_{-0.4}$
(E)	1.03 (165)	2.16(20)	–	144(3)	$0.577^{+0.013}_{-0.012}$	$1.361^{+0.015}_{-0.016}$	$5.4^{1.4}_{-1.1}\times10^{-13}$	–	2.5(4)
(F)	1.02 (165)	$3.4^{+0.4}_{-0.3}$	36(4)	150(5)	–	$1.270^{+0.018}_{-0.019}$	$1.2^{+1.9}_{-0.6}\times10^{-11}$	310^{+320b}_{-150}	$2.4^{+0.4}_{-0.3}$

Notes. Errors are 1σ confidence levels. All tbabs models assume Wilms et al. (2000) abundances. Models: (A) tbabs(bbody); (B) tbabs(bbody+bbody); (C) vphabs(bbody), with best-fit oxygen overabundance of $Z_{\rm O} = 1.60(7)$ in solar units; (D) vphabs(bbody+gauss), with $Z_{\rm O} = 1.64(12)$, best-fit Gaussian $\sigma \sim 0.2$ keV, and line equivalent width of $EW \sim 220$ eV; (E) tbabs(bbody+gauss+gauss), with fixed Gaussian $\sigma_1 = 0.1$ keV and $\sigma_2 = 0.2$ keV, and $EW_1 \sim 90$ eV and $EW_2 \sim 120$ eV; (F) tbabs(bbody+bbody+gauss), with fixed Gaussian $\sigma_2 = 0.2$ keV and $EW_2 \sim 210$ eV. (‡) The unabsorbed flux is in energy band 0.2–12 keV. (†) The radiation radii are estimated normalising the distance to the source to that of Eta Carinae, $d_{\rm Car} = 2.3$ kpc. (a) In order to constrain $R_1^\infty = 20$ km, the source must be at 10 pc ($R_2^\infty \sim 2$ km). (b) In order to constrain $R_1^\infty = 20$ km, the source must be at 150 pc ($R_2^\infty \sim 2$ km).

physical solutions for the neutron star. For double-temperature nsa and nsmaxg models, we fixed the mass of the neutron star at 1.4 $M_\odot$, let the radii ($R_{\rm ns}$ or $R_{\rm em}$) of the two components vary independently of each other, and limited the distance to the source to within 10 pc and 50 kpc. The mass, magnetic field, and distance normalisation of the second thermal component were set equal to those of the first.

The analysis confirms the results of Pires et al. (2012), with much improved count statistics. Overall, the spectrum of the source is soft and purely thermal. However, significant deviations from a Planckian shape are identified around energies 0.55 keV and 1.35 keV (see top plot of Fig. 2). The residuals are present independently of the choice of the thermal continuum, abundance table, source or background extraction regions, as well as regardless of the EPIC instrument and *XMM-Newton* observation.

The best-fit absorbed blackbody (A) has $kT = (133.1 \pm 1.9)$ eV and $N_{\rm H} = (3.20 \pm 0.15) \times 10^{21}$ cm^{-2}, with $\chi^2_\nu = 1.981$ for 169 degrees of freedom (d.o.f.) (Table 4). The column density is consistent with the one towards Eta Carina, $N_{\rm H} \sim 3 \times 10^{21}$ cm^{-2} (Leutenegger et al. 2003). Assuming the neutron star is at a comparable distance, $d_{\rm Car} = 2.3$ kpc (Smith 2006), the redshifted radiation radius derived from the blackbody fit is $R_\infty = (3.8^{+0.5}_{-0.4})(d/d_{\rm Car})^{-1}$ km. We note that the redshifted radiation radii of the M7, as derived from X-ray blackbody fits and distance estimates, are in the range of roughly 2 km to 7 km (see, for example, Kaplan 2008). The residuals mentioned above mostly contribute to the high value of chi-square.

Similarly, if the residuals are not taken into account by adding more spectral complexity, atmosphere models do not provide good fits or plausible physical parameters for J1046. This is illustrated by fits (a) in Table 5 and 6, which consist of simply absorbed nsa and nsmaxg models respectively, with fixed element abundances (no carbatm model provided a fit with $\chi^2_\nu < 10$). The fits lead to inconsistent column densities, sizes of the emission region, and distances; the quality is poor ($\chi^2_\nu = 1.6$–1.9, for 166 to 169 d.o.f.) and several parameters are unconstrained. The effective temperature of magnetised nsa models is usually above 10^6 K as they consist of fully-ionized hydrogen atmospheres. The only nsmaxg models with $\chi^2_\nu < 2$ consist of cold, $T_{\rm eff} \sim (4$–$5) \times 10^5$ K, partially-ionized hydrogen atmospheres, under moderately strong magnetic fields of $B \sim (2$–$3) \times 10^{13}$ G. The large column density, $N_{\rm H} \sim (5$–$7) \times 10^{21}$ cm^{-2}, is inconsistent with a best-fit distance of only ~60 pc. We verified that other element atmospheres (C, O, and Ne) in nsmaxg do not improve the spectral fitting.

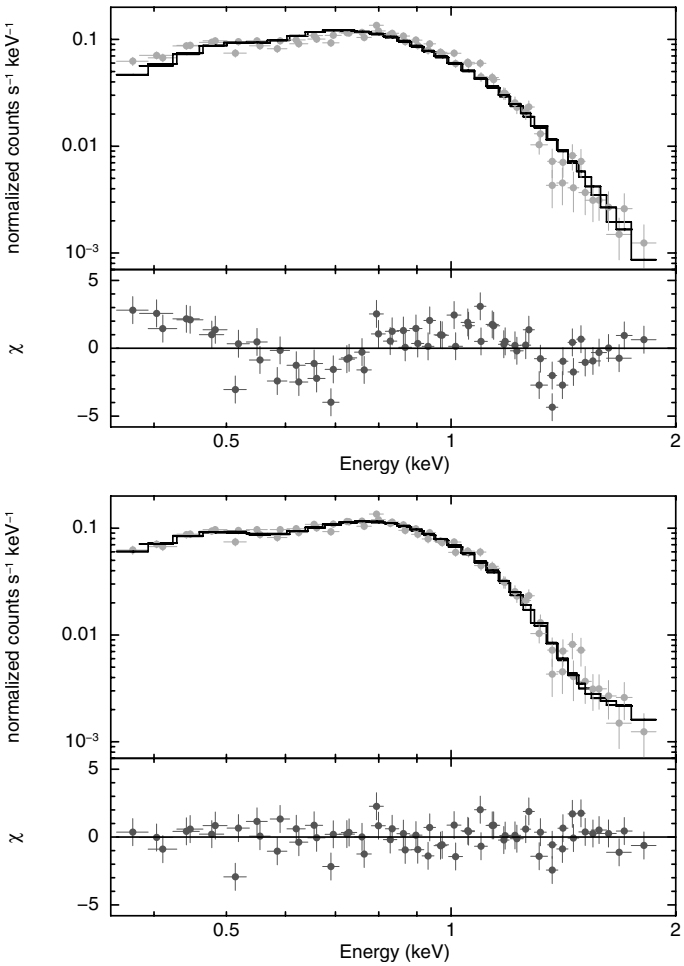

Fig. 2. Results of spectral fitting of source 2XMM J104608.7-594306. We show the two pn spectra and folded best-fit models, with residuals. *Top*: simple absorbed blackbody. *Bottom*: best-fit neutron star atmosphere at $d \sim 2$ kpc ($B = 10^{12}$ G, $T_{\rm eff} \sim 10^6$ K, $N_{\rm H} = 2.6 \times 10^{21}$ cm^{-2}). Two Gaussian lines in absorption are added to the model (with energies around 0.55 keV and 1.35 keV).

Table 5. Results of spectral fitting of neutron star atmosphere models (nsa).

Model	B (G)	χ^2_ν (d.o.f.)	$N_{\rm H}$ (10^{21} cm^{-2})	$T_{\rm eff,1}$ (10^5 K)	$T_{\rm eff,2}$ (10^5 K)	ϵ_1 (keV)	EW_1	ϵ_2 (keV)	EW_2	$M_{\rm ns}$ ($M_\odot$)	$R^\infty_{\rm em,1}$ (km)	$R^\infty_{\rm em,2}$ (km)	$\log(L_{\rm X})$ (erg s^{-1})	d (kpc)
(a)	0	1.92 (169)	4.85(11)	$4.38^{+0.21}_{-0.18}$	–	–		–		1.4	13	–	$31.42^{+0.08}_{-0.07}$	0.17
	1e12	1.63 (169)	$2.59^{+0.13}_{-0.15}$	$30.0^{+4}_{-2.3}$	–	–		–		2	18	–	$34.44^{+0.22}_{-0.14}$	$8.0^{+1.8}_{-6}$
	1e13	1.81 (169)	$3.70^{+0.16}_{-0.23}$	$21.2^{+1.3}_{-2.9}$	–	–		–		2.5	25	–	$34.00^{+0.11}_{-0.26}$	2.58(4)
(b)	0	2.19 (166)	$4.79^{+0.10}_{-0.18}$	$3.00^{+0.12}_{-0.21}$	10	–		–		1.4*	$22.5^{+0.6}_{-0.9}$	6	$32.34^{+0.05}_{-1.1}$	$0.335^{+0.004}_{-0.03}$
	1e12	1.68 (166)	$2.84^{+0.20}_{-0.14}$	$4.4^{+2.7}_{-1.7}$	$24.58^{+0.24}_{-0.5}$	–		–		1.4*	23	6	$33.82^{+0.06}_{-0.04}$	$3.85^{+0.08}_{-0.04}$
	1e13	1.96 (166)	$4.71^{+0.17}_{-0.26}$	$3.1^{+0.8}_{-0.5}$	$13.52^{+0.13}_{-0.12}$	–		–		1.4*	23	6	$32.794^{+0.04}_{-0.024}$	$0.509^{+0.010}_{-0.005}$
(c)	0	1.57 (165)	4.98(11)	$4.41^{+0.26}_{-0.22}$	–	–		–		1.5	13	–	$31.39^{+0.10}_{-0.09}$	0.12
	1e12	1.32 (165)	$2.78^{+0.13}_{-0.20}$	33^{+3}_{-4}	–	–		–		1.9	18	–	$34.53^{+0.15}_{-0.26}$	7^{+3}_{-5}
	1e13	1.89 (165)	$6.34^{+0.19}_{-0.3}$	$4.8^{+1.3}_{-0.4}$	–	–		–		0.8	11	–	$31.5^{+0.4}_{-0.6}$	0.10
(d)	0	1.39 (166)	2.80(3)	$4.3^{+1.5}_{-1.8}$	$15.1^{+2.7}_{-4}$	–		1.346(15)	0.3	1.4*	23	$6.099^{+0.025}_{-0.016}$	$33.1^{+0.3}_{-0.5}$	$1.93^{+0.25}_{-0.23}$
	1e12	1.15 (166)	$1.49^{+0.22}_{-0.13}$	6(4)	38^{+9}_{-4}	–		$1.209^{+0.012}_{-0.014}$	0.25	1.4*	23	6	35(5)	$13.8^{+0.6}_{-0.4}$
	1e13	1.28 (166)	$2.58^{+0.23}_{-0.10}$	$4.1^{+4}_{-0.6}$	$22.6^{+0.3}_{-0.4}$	–		$1.309^{+0.012}_{-0.013}$	0.2	1.4*	23	6	$33.68^{+0.07}_{-3}$	$3.30^{+0.09}_{-0.04}$
(e)	0	1.08 (165)	2.9(3)	$6.3^{+0.5}_{-0.3}$	–	$0.548^{+0.017}_{-0.013}$	0.07	$1.327^{+0.019}_{-0.028}$	0.26	1.4*	13	–	$32.05^{+0.14}_{-0.10}$	0.654(6)
	1e12	1.05 (165)	$2.59^{+0.21}_{-0.3}$	$10.1^{+0.8}_{-0.4}$	–	$0.549^{+0.013}_{-0.014}$	0.07	$1.320^{+0.017}_{-0.014}$	0.22	1.4*	13	–	$32.87^{+0.13}_{-0.07}$	1.997(19)
	1e13	1.12 (165)	$2.91^{+0.20}_{-0.4}$	$9.4^{+0.4}_{-0.5}$	–	$0.545^{+0.013}_{-0.011}$	0.08	$1.352^{+0.014}_{-0.016}$	0.28	1.4*	13	–	$32.75^{+0.08}_{-0.09}$	$1.524^{+0.015}_{-0.014}$

Notes. Errors are 1σ confidence levels (unconstrained parameters are shown with no errors for illustrative purposes). All tbabs models assume Wilms et al. (2000) abundances. All listed models consist of hydrogen atmospheres. Models: (a) tbabs(nsa); (b) tbabs(nsa+nsa); (c) vphabs(nsa), with best-fit oxygen overabundance of $Z_{\rm O} \sim 1.3 - 1.7$ in solar units; (d) tbabs(nsa+nsa+gauss), with fixed Gaussian $\sigma_2 = 0.2$ keV; (e) tbabs(nsa+gauss+gauss), with fixed Gaussian $\sigma_1 = 0.1$ keV and $\sigma_2 = 0.2$ keV. $^{(\star)}$ Parameter held fixed during fitting.

Table 6. Results of spectral fitting of neutron star atmosphere models (nsmaxg).

Model	B (G)	χ^2_ν (d.o.f.)	$N_{\rm H}$ (10^{21} cm^{-2})	$T_{\rm eff,1}$ (10^5 K)	$T_{\rm eff,2}$ (10^5 K)	ϵ_1 (keV)	EW_1	ϵ_2 (keV)	EW_2	$M_{\rm ns}$ ($M_\odot$)	$R^\infty_{\rm em,1}$ (km)	$R^\infty_{\rm em,2}$ (km)	$\log(L_{\rm X})$ (erg s^{-1})	d (kpc)
(a)	2e13	1.64 (166)	$7.14^{+0.05}_{-0.06}$	$3.98^{+0.06}_{-4}$	–	–		–		1.1	23	–	$31.92^{+0.03}_{-22}$	0.06
	3e13	1.83 (168)	$5.32^{+0.06}_{-0.05}$	$5.00^{+0.05}_{-5}$	–	–		–		1.4	13	–	$31.65^{+0.02}_{-23}$	0.06
(b)	3e13	1.86 (166)	$5.30^{+0.07}_{-0.09}$	3.2	79.4	–		–		1.4⋆	13	$\ll 1$	30.85	$0.051^{+0.014}_{-0.023}$
(c)	1e10	1.69 (167)	5.46(21)	$3.88^{+0.16}_{-0.15}$	–	–		–		1.4⋆	13	–	31.21(7)	0.09
	7e12	1.92 (167)	$7.03^{+0.22}_{-0.3}$	$5.13^{+0.21}_{-0.14}$	–	–		–		1.4⋆	13	–	$31.69^{+0.07}_{-0.05}$	0.06
	1e13	1.89 (167)	$6.77^{+0.20}_{-0.29}$	$5.40^{+0.20}_{-0.15}$	–	–		–		1.4⋆	13	–	$31.78^{+0.05}_{-0.06}$	0.08
	3e13	1.56 (167)	5.15(5)	3^{+7}_{-3}	–	–		–		1.4⋆	13	–	$30.9^{+2.0}_{-2.2}$	0.06
(d)	1e10	1.34 (164)	$2.69^{+0.10}_{-0.23}$	$8.59^{+0.16}_{-0.7}$	10	–		$1.360^{+0.013}_{-0.012}$	0.3	1.4⋆	7.7(2.8)	<1.8	$32.1^{+0.8}_{-0.5}$	1.001(8)
	1e12	1.70 (164)	$2.80^{+0.07}_{-0.05}$	3	10	–		$1.391^{+0.008}_{-0.009}$	0.4	1.4⋆	$\ll 2$	2.6	31(24)	0.310(3)
	1.3e12	1.58 (164)	$3.72^{+0.13}_{-0.27}$	$8.36^{+0.13}_{-0.11}$	10	–		$1.369^{+0.010}_{-0.011}$	0.3	1.4⋆	13(4)	<2.0	$32.54^{+0.04}_{-0.3}$	0.975(8)
	2e12	1.58 (164)	$3.78^{+0.15}_{-0.4}$	9	10	–		$1.382^{+0.015}_{-0.011}$	0.3	1.4⋆	$12.4^{+0.6}_{-11}$	<2.3	$32.57^{+0.09}_{-30}$	0.998(3)
	4e12	1.47 (164)	$3.76^{+0.17}_{-0.15}$	3	10	–		1.382(10)	0.3	1.4⋆	$8.6^{+0.6}_{-1.4}$	$0.243^{+0.019}_{-0.016}$	$30.52^{+0.13}_{-22}$	0.03
	7e12	1.42 (164)	3.95(15)	3	10	–		$1.353^{+0.011}_{-0.010}$	0.3	1.4⋆	$12.88^{+0.17}_{-11}$	$0.364^{+0.024}_{-0.022}$	$30.87^{+0.08}_{-24}$	0.05
	1e13	1.41 (164)	$4.02^{+0.17}_{-0.15}$	3	10	–		1.350(11)	0.3	1.4⋆	$10.0^{+0.6}_{-1.3}$	0.254(16)	$30.65^{+0.11}_{-22}$	0.03
	2e13	1.37 (164)	$4.15^{+0.28}_{-0.25}$	3	10	–		$1.346^{+0.012}_{-0.011}$	0.3	1.4⋆	11.7(6)	$0.446^{+0.024}_{-0.05}$	$30.82^{+0.05}_{-0.10}$	0.06
	3e13	1.40 (164)	$3.90^{+0.24}_{-0.25}$	3	10	–		$1.333^{+0.015}_{-0.013}$	0.28	1.4⋆	$12.4^{+0.7}_{-0.8}$	$0.99^{+0.10}_{-0.16}$	$31.02^{+0.11}_{-0.27}$	0.15
(e)	1e10	1.05 (164)	$2.49^{+0.25}_{-0.27}$	$7.7^{+0.6}_{-0.5}$	–	0.554(14)	0.07	1.349(16)	0.27	1.4⋆	9	–	$32.06^{+0.12}_{-0.11}$	0.844(7)
	1e12	1.21 (164)	$3.29^{+0.4}_{-0.29}$	7.4(5)	–	$0.525^{+0.012}_{-0.009}$	0.08	$1.368^{+0.012}_{-0.014}$	0.3	1.4⋆	11	–	$32.20^{+0.11}_{-0.13}$	0.579(5)
	1.3e12	1.20 (164)	$3.21^{+0.3}_{-0.26}$	7.9(5)	–	$0.528^{+0.006}_{-0.009}$	0.08	$1.366^{+0.012}_{-0.013}$	0.3	1.4⋆	11	–	$32.30^{+0.10}_{-0.11}$	0.702(6)
	2e12	1.19 (164)	$3.17^{+0.21}_{-0.4}$	$8.4^{+0.4}_{-0.6}$	–	$0.532^{+0.013}_{-0.010}$	0.08	$1.368^{+0.013}_{-0.016}$	0.3	1.4⋆	10	–	$32.37^{+0.09}_{-0.12}$	$0.793^{+0.007}_{-0.006}$
	4e12	1.16 (164)	$3.05^{+0.21}_{-0.04}$	$9.2^{+0.4}_{-0.5}$	–	$0.537^{+0.013}_{-0.010}$	0.08	$1.357^{+0.013}_{-0.015}$	0.29	1.4⋆	9	–	$32.35^{+0.08}_{-0.11}$	0.855(7)
	7e12	1.15 (164)	$3.04^{+0.20}_{-0.4}$	9.4(5)	–	$0.539^{+0.013}_{-0.010}$	0.08	$1.353^{+0.014}_{-0.015}$	0.28	1.4⋆	10	–	$32.49^{+0.08}_{-0.09}$	$1.032^{+0.009}_{-0.008}$
	1e13	1.14 (164)	$3.03^{+0.20}_{-0.4}$	9.5(5)	–	$0.541^{+0.013}_{-0.010}$	0.08	$1.352^{+0.014}_{-0.015}$	0.28	1.4⋆	9	–	$32.47^{+0.08}_{-0.09}$	$1.017^{+0.009}_{-0.008}$
	2e13	1.13 (164)	$2.99^{+0.21}_{-0.4}$	9.6(5)	–	$0.545^{+0.015}_{-0.012}$	0.07	$1.345^{+0.015}_{-0.016}$	0.27	1.4⋆	8.5	–	$32.41^{+0.08}_{-0.09}$	0.996(8)
	3e13	1.08 (164)	$3.21^{+0.21}_{-0.3}$	$8.6^{+0.7}_{-0.4}$	–	0.550(11)	0.08	$1.313^{+0.021}_{-0.017}$	0.20	1.4⋆	12	–	$32.51^{+0.13}_{-0.08}$	0.956(8)

Notes. Errors are 1σ confidence levels (unconstrained parameters are shown with no errors for illustrative purposes). All tbabs models assume Wilms et al. (2000) abundances. Only results of models with $\chi^2_\nu < 2$ are shown. All listed models consist of hydrogen atmospheres. Models: (a) tbabs(nsmaxg); (b) tbabs(nsmaxg+nsmaxg); (c) vphabs(nsmaxg), with $Z_{\rm O} \sim (1.2-1.3)$; (d) tbabs(nsmaxg+nsmaxg+gauss), with fixed Gaussian $\sigma_2 = 0.2$ keV; (e) tbabs(nsmaxg+gauss+gauss), with fixed Gaussian $\sigma_1 = 0.1$ keV and $\sigma_2 = 0.2$ keV. $^{(\star)}$ Parameter held fixed during fitting.

To test a multi-temperature spectral distribution, we next tried adding one extra thermal component to the absorbed blackbody and atmosphere models. With respect to (A), we obtain an improved fit quality (by $\Delta\chi^2_\nu \sim 0.6$), and blackbody temperatures of $kT_1^\infty = 28.6^{+2.3}_{-2.1}$ eV and $kT_2^\infty = (117.8 \pm 2.2)$ eV (B). However, the large column density of $N_\mathrm{H} = (5.3 \pm 0.3) \times 10^{21}$ cm^{-2} requires the model normalisation of the soft component to be large (the unabsorbed flux is nearly three orders of magnitude higher than that of a single-temperature blackbody). At 2.3 kpc, the radiation radius of the soft component, $R_1^\infty \sim 4000$ km, is inconsistent with that of a compact object. Even if the neutron star is in the foreground of the Carina complex, it should be at a maximum distance of 10 pc from the Sun to constrain $R_1^\infty \lesssim 20$ km. Considering the large N_H of the model, the low galactic latitude of the source, and a chance alignment with the Carina nebula, the solution is unlikely.

A second thermal component in the atmosphere models worsens the chi-square (b). Nonetheless, in spite of a rather poor fit ($\chi^2 \sim 1.7$ for 166 d.o.f.), one solution is more physical, the nsa model for $B = 10^{12}$ G, with $N_\mathrm{H} \sim 2.84^{+0.20}_{-0.14} \times 10^{21}$ cm^{-2}, $kT_1^\infty = 34^{+21}_{-13}$ eV and $kT_2^\infty = 188.6^{+1.9}_{-4}$ eV, at a best-fit distance of ~3.9 kpc. The best-fit radiation radii are, however, pegged at their boundary values of $R_1^\infty = 20$ km and $R_2^\infty = 5$ km. All other (b) models in Tables 5 and 6 show large χ^2_ν, high N_H, and distances below 500 pc.

In (C)/(c), we found that the agreement between model and data is improved below 0.7 keV (typically by $\Delta\chi^2_\nu \sim 0.3$–$0.5$), by allowing oxygen to be extrasolar, with $Z_\mathrm{O} \sim 1.2$–1.6 in solar units, depending on the choice of continuum. In general, there is no significant change in the best-fit parameters (the exception is for the nsa model with for $B = 10^{13}$ G). Despite the improvement, all nsmaxg models (c) still show large N_H and distances contradictorily below 100 pc, regardless of the magnetic field strength. The abundance of oxygen was the only one tightly constrained by the vphabs fits, which were found to be either insensitive to other elements (e.g. C, Ne, Si, or Fe), or to produce large overabundances (e.g. N, Mg, and Ca). In particular, elements with lines around 1.35 keV were verified to be arbitrarily overabundant in the model. A variable absorption model, combined with a double-temperature blackbody, has no effect on the elemental abundances, which are insensitive to the fit. This is likely due to the fact that the two blackbody components cross around an energy of 0.5 keV, where the vphabs model tries to accomodate for the extrasolar amount of oxygen.

Independently of the continuum – single or double-temperature, blackbody or atmosphere, with fixed or overabundant elements – we verified that the introduction of a Gaussian line in absorption around an energy of 1.35 keV significantly improves the quality of the spectral fitting. With respect to (C), the presence of the line improves the fit by $\Delta\chi^2_\nu \sim 0.4$, resulting in a less absorbed model, with $N_\mathrm{H} = 2.17^{+0.22}_{-0.20} \times 10^{21}$ cm^{-2} and $kT = (157 \pm 5)$ eV (D). The oxygen abundance is similar, $Z_\mathrm{O} = (1.64 \pm 0.12)$, and a best-fit line energy is centred at $\epsilon = 1.289^{+0.018}_{-0.017}$ keV, with equivalent width $EW \sim 220$ eV. Similar parameters and chi-square values are obtained when, alternatively, the abundances are fixed, and two lines in absorption are added to the blackbody continuum (E). In this case, the best-fit line energies are centred at $0.577^{+0.013}_{-0.012}$ keV, and $1.361^{+0.015}_{-0.016}$ keV and have equivalent widths of 90 eV and 120 eV. (To better constrain the model parameters, the Gaussian σ of the two components were held fixed to 0.1 keV and 0.2 keV, respectively.)

As for (B), the presence of a line at $\epsilon = 1.270^{+0.018}_{-0.019}$ keV results in a lower flux normalisation and a column density consistent with that towards Carina, $N_\mathrm{H} = 3.4^{+0.4}_{-0.3} \times 10^{21}$ cm^{-2} (F); the fit quality is improved by $\Delta\chi^2_\nu \sim 0.3$ and the temperature of the two components are higher ($kT_1^\infty = 36 \pm 4$ eV and $kT_2^\infty = 150 \pm 5$ eV). Still, the neutron star should be at a maximum distance of 150 pc to constrain $R_1^\infty \lesssim 20$ km. Regarding the double-temperature atmosphere models, the presence of the absorption line at ~ 1.35 keV also results in solutions with more consistent physical parameters (d). In particular for nsa with $B = 0$ G and $B = 10^{13}$ G, the column density is $N_\mathrm{H} = (2.6$–$2.8) \times 10^{21}$ cm^{-2} and the distance is within $d \sim 1.9$ kpc to 3.3 kpc, i.e. consistent with a neutron star in Carina. The best-fit solutions have $kT_1^\infty \sim 30$ eV and $kT_2^\infty = 120$–170 eV, with $R_1^\infty \sim 20$ km and $R_2^\infty \sim 5$ km.

Finally, we tested a combination similar to that in (E), i.e. a single-temperature model with two lines, for the nsa and nsmaxg models. These are models (e) in Table 5 and 6, respectively, which are also the ones with the lowest-χ^2 values in the analysis. Interestingly, all relevant parameters show best-fit values in a much narrower range. The energy of the lines are centred at $\epsilon_1 \sim 0.55$ keV and $\epsilon_2 \sim 1.31$–1.37 keV, and the equivalent widths are $EW_1 \sim 72$–81 eV and $EW_2 \sim 200$–300 eV. As for (E), the Gaussian σ of the two components was fixed. Canonical M_ns and R_ns values typically provided the least chi-square fits. The size of the redshifted emitting region is within 8.5 km and 13 km – overall consistent with the emission originating from most of the surface. The magnetic field intensity is not constrained by the atmosphere models, as the least-χ^2 fits have $B = (0$–$3) \times 10^{13}$ G. In the lower plot of Fig. 2, we show the two pn spectra folded with the best-fit nsa model (e), for $B = 10^{12}$ G.

In Table 7 we summarise the best-fit parameters of this same model for the six individual EPIC spectra. The results are consistent overall. The most deviant parameters result from fitting the MOS2 spectrum of the AO9 observation. Indeed, this spectrum was not considered in the analysis of Pires et al. (2012).

The inclusion of power-law tails extending towards higher energies has no effect on the parameters of the least-χ^2 models. Considering again the best-fit nsa model (e), we found that non-thermal power-law components with typical photon indices of $\Gamma = 1.7$–2.1 (see, for example, De Luca et al. 2005) contribute at most 0.5 % (3σ confidence level) to the luminosity of the source.

Table 7. Best-fit parameters per observation and EPIC camera.

	$N_\mathrm{H}{}^\dagger$ ($\times 10^{21}$)	T_eff ($\times 10^5$ K)	ϵ (keV)	d (kpc)
(1)	$2.9^{+0.5}_{-0.4}$	$9.3^{+1.0}_{-0.9}$	$0.569^{+0.028}_{-0.025}$, 1.32(3)	$1.5^{+0.6}_{-0.5}$
(2)	$2.3^{+1.2}_{-1.0}$	$9.1^{+4}_{-2.1}$	$0.516^{+0.025}_{-0.021}$, 1.40(13)	$1.5^{+1.5}_{-0.8}$
(3)	$4.9^{+1.5}_{-1.1}$	$8.6^{+1.2}_{-1.7}$	0.80(5), $1.24^{+0.08}_{-0.07}$	$0.9^{+0.4}_{-0.3}$
(4)	$2.2^{+0.4}_{-0.5}$	$11.1^{+1.6}_{-1.0}$	$0.544^{+0.022}_{-0.019}$, $1.295^{+0.024}_{-0.025}$	$2.7^{+0.6}_{-0.7}$
(5)	$3.1^{+0.9}_{-0.8}$	$9.4^{+1.4}_{-1.6}$	$0.59^{+0.04}_{-0.03}$, 1.33(5)	$1.4^{+0.9}_{-0.6}$
(6)	$3.3^{+1.3}_{-1.1}$	$9.1^{+1.8}_{-1.4}$	$0.52^{+0.10}_{-0.04}$, 1.32(5)	$1.3^{+0.7}_{-0.5}$

Notes. Errors are 1σ confidence levels. The fitted model is (e) for a nsa with $B = 10^{12}$ G (see Table 5). The fitted spectra are (1) pn AO9; (2) MOS1 AO9; (3) MOS2 AO9; (4) pn AO11; (5) MOS1 AO11; (6) MOS2 AO11. The reduced chi-square values range between 0.6 to 1.5. $^{(\dagger)}$ The column density is in cm^{-2}.

3.2. Timing analysis

To reassess the significance of the periodic signal detected at $P \sim 18.6$ ms, we restricted the timing analysis to the pn data and

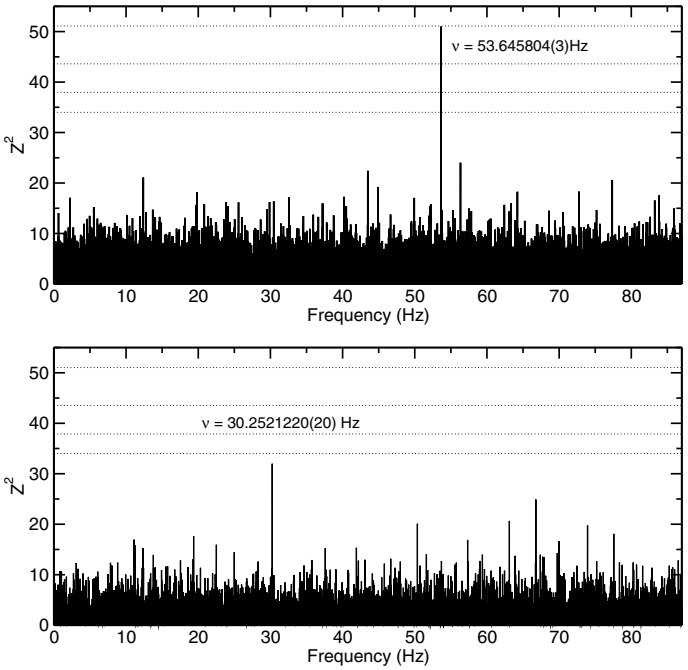

Fig. 3. Results of Z_1^2 tests in the AO9 (*top*) and AO11 (*bottoms*) pn time series. The frequency range is $\Delta\nu \sim 87.7$ Hz. Dashed horizontal lines show confidence levels of 1σ to 4σ (68% to 99.994%) for the detection of a periodic signal, taking the whole frequency range of the search into consideration (see text). The frequency of the highest peak resulting from each search is labelled. *Top*: the energy band is 0.36−2.25 keV, the size of the extraction region is 18.6″, and the number of photons is 5188. *Bottom*: the energy band is 0.37−1.9 keV, the size of the extraction region is 19.7″, and the number of photons is 5244.

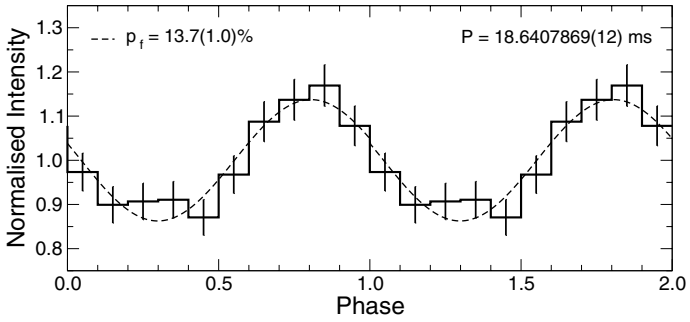

Fig. 4. AO9 pn light curve, folded at $P \sim 18.6$ ms (the epoch of phase zero is defined at T_0 = MJD 5536.00884 days). The energy band is 0.36−2.25 keV and the size of the extraction region is 18.6″. Two cycles are shown for clarity. The best-fit sinusoidal function is also shown (dashed line).

completely reanalysed the AO9 dataset consistent with the new *XMM-Newton* observation. We considered events with photon patterns 12 or lower and tested different energy bands and radii of the source extraction region; the purpose was to unveil potential pulsations from the neutron star by minimising the background contribution. The spatial and energy selection cuts provide roughly $N_{\rm ph} \sim (4{-}6) \times 10^3$ pn events in each observation.

Each pn time series was Fourier-analysed in frequency domain to search for the presence of periodic signals. The Z_n^2 (Rayleigh) statistic (Buccheri et al. 1983) was computed directly on the photon times-of-arrival; these were converted from the local satellite to the solar system barycentric frame using the SAS task barycen and the source coordinates in each pn observation (Table 2). We adopted a step in frequency of 2 μHz (or an oversampling factor of the expected width of the Z_n^2 peaks of nearly 10), warranting that a periodic signal is not missed in our searches. The number of statistically independent trials in each Z^2 test is estimated as $\mathcal{N} = \Delta\nu t_{\rm exp} \sim 8 \times 10^6$, with $\Delta\nu \sim 87.7$ Hz and $t_{\rm exp} \sim 87$ ks to 90 ks. In the absence of a periodic component, the mean and standard deviation of the Z_n^2 values, with $n = 1$, are equal to 2, as the Z_1^2 statistic is distributed as a χ^2 with two degrees of freedom. Therefore, the probability of obtaining a noise peak of a given power Z^2 in $\mathcal{N}$ independent trials is given by $\alpha = \mathcal{N} \exp(-Z^2/2)$; the confidence level of a detection can then be established as $C = (1 - \alpha) \times 100\%$.

The analysis of the AO9 dataset yields only one statistically significant periodic signal, at $\nu_* = 53.645804(3)$ Hz ($P_* = 18.6407869(12)$ ms; see top plot of Fig. 3). The power of the Z_1^2 statistic at ν_* is energy and signal-to-noise (S/N) dependent, being measured at best (or most significantly) when photons with energy below ~0.35 keV (where the noise of the pn camera in SW mode dominates) are excluded from the analysis, or when the source extraction region is around an optimal value between 17″ and 22″. These reflect the intervals where the S/N ratio is optimal, indicating an origin on the neutron star itself.

The measured fluctuation of the power of the Z_1^2 statistic at ν_*, $Z_1^2(\nu_*) \sim 36{-}50$, is consistent with that expected from a sinusoidal modulation of amplitude $p_{\rm f} = (12.5 \pm 1.9)\%$ (see, for example, Pavlov et al. 1999). Indeed, this is the amplitude derived from a sinusoidal fit of the light curve of the pn camera, folded at $P = P_*$ (Fig. 4); the pulsed fraction is also consistent with the non-parametric determination of the signal strength, $p_{\rm f} = (13.1 \pm 1.6)\%$, computed directly from the sample phases according to the bootstrap method proposed by Swanepoel et al. (1996).

The inclusion of higher harmonics $n \geq 2$ in the Z_n^2 test was found to be statistically insignificant. Extensive searches showed no other significant signal (above the 1σ confidence level, or with $Z_1^2 > 34$) across the frequency range of the analysis, and safety checks did not suggest an unknown instrumental or background origin for the periodic signal at ν_* (see Pires et al. 2012, for details). We also verified that the periodic signal is always present at the same frequency, independently of the details on the processing of the raw event file (e.g. included calibration files, SAS version, randomisation in energy within a PI channel, event filtering, or randomisation in time within the sampling detector time).

In the AO11 dataset, however, no obviously significant candidate frequency results from our Z_n^2 tests. Extensive tests positively exclude modulations with $p_{\rm f} > 14\%$ ($Z_1^2 > 51$, 4σ) in the $\nu = (0.01{-}87.73)$ Hz frequency range of the search. However, at the brightness level of J1046, a modulation with $p_{\rm f} = 11\%$ to 13% may be missed in searches with too large a number of trials. As the background level in the second observation is higher and the exposure time slightly shorter, the pulsed signal at P_* may have been more severely affected (or smeared out) by noise. Alternatively, the AO9 signal is spurious and/or unrelated with the spin period of the neutron star (see discussion in Sect. 4.1).

By considering $\Delta\nu = 87.7$ Hz, the only signal that shows a Z_1^2 power above the 1σ confidence level – regardless of the energy band of the search – is at $\nu_{\rm AO11} = 30.252122(22)$ Hz (see lower plot of Fig. 3). The measured fluctuation in our tests is $Z_1^2 = 22{-}39$, consistent with a pulsed fraction of $p_{\rm f} = 11.5(9)\%$. The overall signficance of the signal is low: on average, the probability of obtaining such a peak by chance is ~23%. Furthermore,

the shift in frequency with respect to the first *XMM-Newton* observation is too large ($\nu_* - \nu_{\rm AO11} \sim 23.4$ Hz) for the two signals to be associated. The implied spin-down rate would produce, within the usual magneto-rotational dipole-braking scenario in a vacuum, a magnetic field of $B_{\rm dip} = 6.6 \times 10^{13}$ G. In particular, a field with $B > 5 \times 10^{12}$ G would spin down the pulsar at a rate >0.1 Hz yr^{-1}, making the detection of a very short period of ~20 ms unlikely in the first place.

Regardless of the absence of an obvious candidate periodicity, the new *XMM-Newton* observation can still be used in combination with the AO9 data in a coherent two-dimensional $Z_1^2(\nu, \dot{\nu})$ search, i.e. allowing the Z_n^2 test to account for the neutron star spin-down. In this case, the ephemeris parameters $(\nu, \dot{\nu})$ that determine the phase ϕ_j of each photon time-of-arrival,

$$\phi_j = \nu(t - t_0) + \dot{\nu}\frac{(t_j - t_0)^2}{2} \qquad j = 1, \ldots, N_{\rm ph},$$

are estimated as the values that give the highest power of the Z_1^2 statistic. Here, t_0 is the event time-of-arrival counted from an epoch of phase zero and $N_{\rm ph} = 10\,355$ is the total number of photons in the search, when joining the two datasets for the optimal choices of energy band and extraction region.

We searched for significant Z_1^2 peaks in an interval of $\pm 5\sigma$ around ν_*, in steps of 5×10^{-9} Hz, and explored frequency derivatives from -1×10^{-18} Hz s^{-1} up to a maximum of $\dot{\nu}_{\rm max} = -1 \times 10^{-10}$ Hz s^{-1}, in steps of -2×10^{-16} Hz s^{-1}. The choice of the maximum frequency derivative is reasonable, as only three isolated pulsars – the Crab and the energetic pulsars PSR J0537-6910 and PSR J0540-6919 in the Large Magellanic Cloud, out of about 2400 known objects – are known to slow down at a rate faster than $\dot{\nu}_{\rm max}$. The number of independent trials is given by $\mathcal{N} = (\nu_{\rm max} - \nu_{\rm min})|\dot{\nu}_{\rm max} - \dot{\nu}_{\rm min}|T_{\rm span}^3/2 \sim 4 \times 10^8$, where $T_{\rm span} = 6.4 \times 10^7$ s is the time span between the AO9 and AO11 observations.

We found that the power of the Z_1^2 statistic increases significantly when folding the two datasets, even though the number of trials is boosted by a factor of 100. The highest peak resulting from our search, with $Z_1^2 \sim 58$, occurs at $\nu = 53.645805460(5)$ Hz and $\dot{\nu} = -2.536200(15) \times 10^{-11}$ Hz s^{-1} (T_0 = MJD 55 536.008840 days is the epoch of phase zero); the chance probability of the solution considering all number of independent trials is 0.01% (confidence level of 3.885σ). A total of 17 solutions, out of $\sim 6 \times 10^9$, were found at or above the 3σ level (with $51.5 \lesssim Z_1^2 \lesssim 58$); none was above the 4σ level. All high-Z_1^2 solutions have frequency derivatives within $-9.8 \times 10^{-11} \lesssim \dot{\nu} \lesssim -1.2 \times 10^{-11}$ Hz s^{-1}. Within the scenario of magnetic braking in vacuum, the spin-down values imply a dipolar field of $B_{\rm dip} = (3\text{–}8) \times 10^{11}$ G for the source.

To test the result beyond its formal significance, we reproduced (in full resolution and over the same parameter space) the two-dimensional $Z_1^2(\nu, \dot{\nu})$ search, but folded AO11 events extracted from a background region over the original AO9 time series of the source. The background region was scaled to have roughly the same number of counts as collected for J1046, and two different energy bands were tested: the 0.36–2.2 keV of the original search, where the S/N ratio is optimal, and the 3–10 keV energy band, which aims at excluding contamination from the neutron star. The goal is to verify empirically the power of the Z_1^2 statistic on a search with similar sensitivity, total duration, and time span of the original one, but conducted over the times of arrival of noise events that should not relate with the periodic signal at ν_*.

We found that Z_1^2 peaks of similar power are obtained on these tests for intervals of frequency derivative that are roughly of the same order as those of the original search. In the 0.36–2.2 keV energy band, we found 14 solutions above the 3σ level (again out of $\sim 6 \times 10^9$ grid points), with $Z_1^2 \sim (51.5\text{–}61)$ and $-3 \times 10^{-11} \lesssim \dot{\nu} \lesssim -8 \times 10^{-12}$ Hz s^{-1}. The highest Z_1^2 power occurs at $\dot{\nu} \sim -8 \times 10^{-12}$ Hz s^{-1} and implies $B_{\rm dip} \sim 2.3 \times 10^{11}$ G. For the 3–10 keV energy band, 28 solutions with frequency derivatives in the range $-7 \times 10^{-11} \lesssim \dot{\nu} \lesssim -1.2 \times 10^{-11}$ Hz s^{-1} were found with $Z_1^2 \sim (51.5\text{–}60)$, and the highest power is for $\dot{\nu} \sim -7 \times 10^{-11}$ Hz s^{-1}, which implies $B_{\rm dip} \sim 7 \times 10^{11}$ G. The tests show that the high Z_1^2 power is likely to be caused by statistical fluctuations in a search with a large number of trials and that the best $(\nu, \dot{\nu})$ solution derived for J1046 is not significant.

4. Discussion

4.1. Summary of results

At present, we cannot rule out the possibility that the periodic signal at $P_* \sim 18.6$ ms, which was only significantly detected in the AO9 observation ($p_{\rm f} = 12.5(1.9)\%$, c.l. 3σ to 4σ, depending on the S/N ratio of the search; see Sect. 3.2) is unrelated to the true spin period of the neutron star. The second *XMM-Newton* observation proved inconclusive at confirming the fast candidate spin, providing an upper limit that is close to the limiting sensitivity for detecting the AO9 modulation ($p_{\rm f} < 14\%$ at 4σ, for $P = 0.0114\text{–}100$ s and 0.35–2 keV). No other periodic signal was found to be statistically significant in extensive searches performed over the individual datasets (in a wide frequency range and for different tested energy bands). In particular, pulsations with $P > 0.6$ s (a range relevant for AXPs, the M7 INSs, and RRATs[1]) are constrained down to $p_{\rm f} \sim 10\%$ (3σ, 0.35–2 keV: Pires et al. 2012). Such smooth X-ray pulsations are usually more frequently observed in the M7 and CCOs, as AXPs typically show $p_{\rm f} \gtrsim 15\text{–}30\%$.

The coherent combination of the two EPIC-pn time series, in a joint periodicity search around the candidate spin and accounting for a wide range of possible pulsar spin-down values, provides a $(P, \dot{P})$ solution with a probability of 1 in 10 000 of it being spurious. Across the searched parameter space, the solutions above 3σ imply a dipolar magnetic field of $B_{\rm dip} = (3\text{–}8) \times 10^{11}$ G, under the assumption of magnetic braking in vacuum. However, additional tests suggest that the timing solutions are likely to be below their formal statistical significance.

In the absence of a clear period determination and good estimate of the magnetic field, the evolutionary state and nature of this neutron star remain as yet to be constrained. Unfortunately, at the flux level of the source and with current X-ray facilities, pulsations are difficult to detect below the limits provided by present data.

We were nonetheless able to study the spectral properties of J1046 with unprecedented detail and statistics (Sect. 3.1). Interestingly, we found that good fits and meaningful physical parameters are only derived when the residuals at energies 0.55 keV and 1.35 keV are taken into account by the spectral modelling. Independently of the exact choice of the thermal continuum, we found that the former residuals may result either from a local overabundance of oxygen in the Carina nebula

[1] As of 2015, over 1000 sources in the ATNF pulsar catalogue (of which 30 are X-ray pulsars and 58 are RRATs) are known to spin at periods longer than 0.6 s (Manchester et al. 2005).

(with $Z_O = 1.2-1.7$, relative to solar) or from the inhomogenous temperature distribution on the surface of the neutron star (the best-fit double-temperature models have $kT_1^\infty = 30-36$ eV and $kT_2^\infty = 120-190$ eV). Phenomenologically, the residuals at 0.55 keV can also be described by a Gaussian absorption line with $EW \sim 70-90$ eV. On the other hand, of all models tested in Sect. 3.1, the residuals at 1.35 keV are only satisfactorily accounted for by invoking a line in absorption, with $EW \sim 120-400$ eV (depending on the choice of the continuum). In this case, the fits lead to overall physically consistent (as well as much more tightly constrained) spectral parameters: $N_H = (2.5-3.3) \times 10^{21}$ cm^{-2}, $T^\infty = (5-8) \times 10^5$ K, $L_X^\infty = (0.7-4) \times 10^{32}$ erg s^{-1}, and $d \sim 1-3$ kpc (considering the solutions with $\chi^2_\nu < 1.4$).

4.2. Comparison with other pulsars

Of all the INSs that clearly show thermal X-ray emission (see, for example, the compilation of Viganò et al. 2013), J1046 displays spectral properties that are quite close to those of the M7 and CCOs – namely, the soft energy distribution, constant X-ray properties on a long timescale ($\gtrsim$15 yr), absence of significant magnetospheric emission, and evidence of absorption features. Deeper radio and γ-ray limits are, however, needed to exclude a middle-aged rotation-powered pulsar (RPP) or a mildly-recycled neutron star (e.g. Belczynski et al. 2010).

The likely presence of J1046 in the Carina open cluster excludes a neutron star much older than $\sim 10^6$ yr (see discussion in Pires et al. 2012). In millisecond pulsars (MSPs), as well as in middle-aged and old RPPs, a considerable fraction of the X-ray emission arises from polar caps, which are heated by back-flowing charges accelerated in the pulsar magnetosphere. The spectral analysis shows that the X-ray emitting region in J1046 is consistent with the surface of a canonical neutron star when realistic atmosphere models are adopted. This is in contrast to the $\sim$0.1 km blackbody radii typically derived for MSPs (e.g. Bogdanov et al. 2006, 2011).

Middle-aged RPPs (e.g. the Three Musketeers, with ages of a few $\sim 10^5$ yr and spin-down power of a few $\sim 10^{34}$ erg s^{-1}) are dominated by thermal emission and show much lower residual magnetospheric activity (at levels within 0.3% and 1.7% of the source luminosity; De Luca et al. 2005). In J1046, no such weak hard tail (above 0.5% of the source luminosity) is present, and we found no compelling evidence for a second (hotter) thermal component, as that typically arising from heated polar caps (see discussion in Sect. 4.3). For most RPPs, the efficiency at converting rotational energy into X-rays is generally above $\eta = 10^{-5}$ (Kargaltsev et al. 2012). By considering the 3σ upper limit on the source non-thermal X-ray luminosity, $L_X^{pl} \lesssim 2 \times 10^{30}$ erg s^{-1} (Sect. 3.1, for the best-fit nsa model (e) and $B = 10^{12}$ G), and assuming a maximum age of 10^6 yr for the neutron star, we can derive a lower limit on the spin-down luminosity of the source, $\dot{E} > 2.1 \times 10^{36}$ erg s^{-1}, if the neutron star is indeed a fast rotator. This implies an exceptionally low efficiency ratio of $\eta \lesssim 10^{-6}$ for J1046, if the neutron star is a typical RPP. Alternatively, if the signal at P_* is not related with the INS spin period, the possibility remains that J1046 is a fainter and more distant M7-like INS.

4.3. Origin of absorption lines

The detection of spectral features in absorption in several (non-accreting) thermally emitting neutron stars – including the M7, CCOs, magnetars, and Calvera – have been widely reported (e.g. Sanwal et al. 2002; Mori et al. 2005; Haberl 2007; McLaughlin et al. 2007; Zane et al. 2011; Tiengo et al. 2013). The physical interpretation is not unique. The features can be due to atomic transitions in the magnetised atmosphere or condensed surface of the neutron star, or be cyclotron lines generated in a hot ionized layer near the surface. Importantly, the central energies of the features have been used to give estimates on the state of magnetisation of the neutron star. Recently, Viganò et al. (2014) showed that, in some cases (as for the M7 RX J0806.4-4123; Haberl et al. 2004), rather than an actual transition between energy levels, the spectral deviation may be induced simply by the inhomogeneous temperature distribution on the surface.

In J1046, we verified that a double-temperature spectral model is only a plausible (physical) solution when we introduce an absorption feature at 1.35 keV. Even in this case, the reduced chi-square values are still high (with respect to single-temperature models) and the radiation radii are uncertain. Possibly, the poor fit reflects the inadequate description of the anisotropic temperature distribution on the surface of a neutron star by the simple superposition of two atmosphere models.

If we assume that the feature at energy $\epsilon \sim 1.35$ keV is the fundamental electron cyclotron absorption, similar to the case of the CCO 1E 1207.4-5209 (Bignami et al. 2003), we can derive an estimate of the magnetic field on the surface for J1046. According to the relation $\epsilon_{cyc} = 1.16(B/10^{11}\,\mathrm{G})(1 + z_g)^{-1}$, we obtain $B_{cyc} \sim 1.5 \times 10^{11}$ G for the gravitational redshift of a canonical neutron star, $z_g \sim 0.3$.

4.4. Association with a runaway star in Carina

A runaway massive star in the Carina nebula, MJ 218 (listed in the UCAC4 catalogue as 153-055048) was recently proposed to have been associated with the progenitor of J1046 in a binary system, which was then disrupted by the supernova explosion that created the neutron star (Ngoumou et al. 2013). At a distance of 2.3 kpc, the 18′ angular separation of the two objects on the sky implies a physical distance of $\sim$12 pc. The total proper motion of the runaway star corresponds to a transverse speed of $v_t = 95 \pm 52$ km s^{-1} (Zacharias et al. 2004). Assuming typical masses of 1.4 $M_\odot$ and 9.6 $M_\odot$ (spectral type B1.5 V; Pecaut & Mamajek 2013), respectively, for the neutron and runaway stars, the estimated flight time is of $t_{kin} \sim (1.1-3) \times 10^4$ yr, which is roughly consistent with the absence of a supernova remnant. Although uncertain, the implied velocity of J1046, $v_t \sim 650 \pm 360$ km s^{-1}, if previously associated with MJ 218, is also consistent with the distribution of transverse speeds observed in non-recycled radio pulsars (Hobbs et al. 2005).

4.5. Thermal evolution

Based on our best-fit spectral solutions, we can investigate the thermal state of the neutron star amidst the several INS populations for the first time. Figure 5 shows a representative sample of INSs, in a cooling-age diagram. The temperature T^∞ is the apparent effective surface temperature, as derived from either atmosphere or blackbody models. Whenever possible, age estimates and intervals are derived from proper motion measurements (flight time) or associations with supernova remnants; otherwise the pulsar spin-down age, uncertain by a factor of two, is adopted. The data on RPPs (14 objects including the Crab and Vela pulsars, as well as the Three Musketeers and the old pulsar PSR J2043+2740) are collected from Yakovlev et al. (2008). The five CCOs in the diagram are the neutron stars in the Cas A,

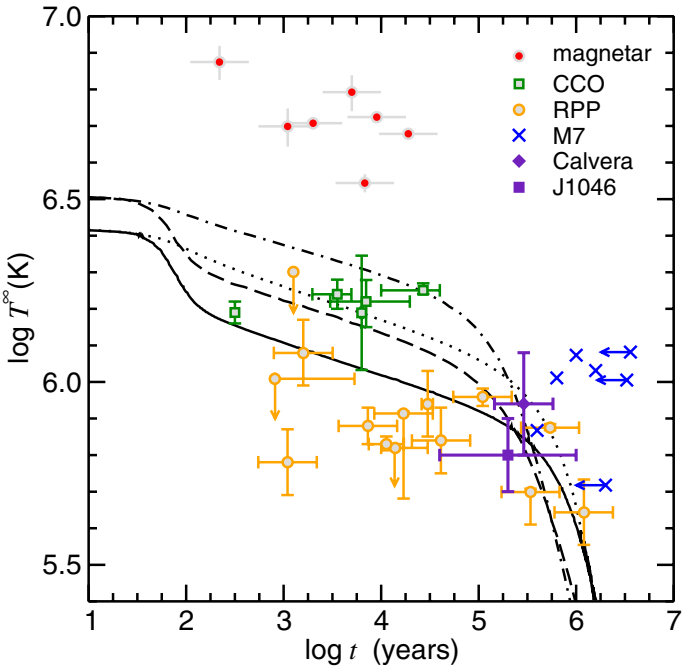

Fig. 5. Cooling-age diagram for different groups of isolated neutron stars (data points: see legend). Theoretical cooling curves for a canonical neutron star are shown as lines (see text). No effects of magnetic field decay are considered.

Puppis A, G296.5, Kes 79, and HESS J1731-347 supernova remnants (Bogdanov 2014; Klochkov et al. 2015, and references therein); in particular, their emission can be interpreted as radiation from the entire surface, using either hydrogen or carbon atmosphere models. The locus of magnetars (SGRs and AXPs) is represented by the seven objects investigated by Kaminker et al. (2009, and references therein). Data points for the M7 are according to the compilations of Kaplan et al. (2011) and Viganò et al. (2013). For these sources, characteristic ages are shown as upper limits on true ages in the absence of a kinematic estimate.

Following our previous discussion, we adopt J1046's flight time as a lower limit for its age estimate; a conservative value of 10^6 yr is taken as an upper limit, based on an association with the Carina nebula. The temperature range is as reported in Sect. 4.3. For Calvera, we adopt the temperature of the best-fit atmosphere (nsa) model (Zane et al. 2011) and the INS characteristic age (again uncertain by a factor of two, Halpern et al. 2013).

The set of theoretical cooling curves in Fig. 5 correspond to four representative families, which are described in, for example, Weisskopf et al. (2011), Yakovlev et al. (2011), Klochkov et al. (2015)[2]. In a nutshell, the so-called standard neutrino candle, represented in Fig. 5 by a solid line, shows the thermal evolution of a canonical neutron star (of mass $M = 1.5\,M_{\odot}$ and radius $R = 12$ km, with a nucleon core), where cooling is governed by the modified Urca process, and an iron envelope is assumed (no enhanced cooling in the first 100 yr). The dotted line shows the same star affected by strong proton superfluidity in the core, which highly suppresses the Urca reactions and results in a hotter neutron star at $t \gtrsim 100$ yr. The dashed and dot-dashed lines are the corresponding (non-superfluid and superfluid) models for a star with a full amount of accreted light elements (in particular, $\Delta M \sim 10^{-8}\,M_{\odot}$ of carbon) in the blanketing envelope. The presence of light elements in the envelope of the neutron star increases the thermal conductivity (Potekhin et al. 1997); as a result, the light-element envelope regulates and slows down the cooling in the first $\sim 10^4$–10^5 yr, depending on the amount and composition of the accreted material. The effect of the magnetic field on cooling is not taken into account, which is a valid approximation for $B \lesssim 10^{12}$ G.

The strong thermal emission (high temperature at a given age) observed in magnetars and the M7, with respect to the standard cooling theory and other INS groups, cannot be explained without taking into account the effects of magnetic field decay as an additional source of heating of the neutron star crust. Magneto-thermal evolutionary models (Viganò et al. 2013) show that, for strongly magnetised INSs, field dissipation keeps the stellar crust hot for a longer time than expected from standard cooling (see, Aguilera et al. 2008, and references therein); moreover, strong fields at birth ($B > 10^{14}$ G) can significantly brake the neutron star spin to an asymptotic value in a relatively short timescale ($\sim 10^5$ yr). Interestingly, whereas for the bulk of the neutron star population such effects are negligible, the model implies an evolutionary link between the M7 and magnetars.

On the other hand, consistent with the standard theory, CCOs are young neutron stars that show the slow cooling in the neutrino-cooling era typical of sources with light-element accreted envelopes. For these neutron stars, the turning point towards the steep drop in temperature of the photon-cooling stage takes place earlier than for neutron stars with an iron envelope. As a result, old CCOs may be invisible to X-ray observations after ~ 1 Myr, where luminosities may have dropped below $\sim 10^{31}$ erg s^{-1}, and surface temperatures are colder than ~ 20 eV to 30 eV. Nuclear burning in the envelope, and hence a change of composition, might nonetheless slow down the cooling in the last stages of the thermal life of the neutron star (Page et al. 2011).

Overall, the cooling status of Calvera appears consistent with a scenario where this neutron star evolved from a CCO (see Sect. 1). However, Calvera's real surface temperature may be considerably softer than the adopted value in Fig. 5, $kT \sim 98$ eV, as the source shows a clear indication of a double-temperature energy distribution (Zane et al. 2011). In particular, the fit with a double thermal (blackbody or nsa) model constrains the apparent temperature of the cooler component within $T^{\infty} \sim (6\text{–}9) \times 10^5$ K, which is very similar to the interval estimated for J1046. Given its resemblance to Calvera, and if the fast spin and indication of a low magnetic field in J1046 are to be confirmed, the INS in Carina may be another potential candidate for the elusive class of evolved anti-magnetars.

5. Summary and conclusions

Following the intriguing detection of a short periodic signal in the neutron star 2XMM J104608.7-594306 (Pires et al. 2012), we targeted the source again with *XMM-Newton*, aiming at better characterising its spectral energy distribution and timing properties. The new *XMM-Newton* dataset unfortunately proved inconclusive in confirming the fast spin of the neutron star. The derived 4σ upper limit on the pulsed fraction, $p_{\rm f} < 14\%$, shows that the observation is just at the limiting sensitivity to detect the modulation found previously.

Without a clear determination of the spin period and a robust estimate of the magnetic field of the neutron star, its exact nature

[2] As noted by Klochkov et al. (2015), these curves are mostly aimed at explaining the residual heating observed in CCOs. Colder neutron stars, like some RPPs in Fig. 5, may be regarded as sufficiently massive stars with higher neutrino luminosity owing to the onset of the direct Urca process in the core.

remains open to interpretation. The INS 2XMM J104608.7-594306 may be similar to Calvera, a neutron star for which the scenario of an evolved anti-magnetar, within the framework of the magnetic field burial by fallback of supernova debris, has been discussed. The overall spectral properties of 2XMM J104608.7-594306 and its likely presence in the Carina open cluster disfavour a recycled object or a standard evolutionary path, typical of that of a rotation-powered pulsar. However, better age estimates (e.g. through kinematic studies), as well as deeper radio and γ-ray limits, are required to further constrain the evolutionary status of this neutron star. In particular, studies in the optical and near-infrared may offer the opportunity to assess properties which, for J1046, are not assessible by other means.

The prospect of finding more thermally emitting isolated neutron stars with the upcoming all-sky survey X-ray mission, *eROSITA* (Predehl et al. 2014; Merloni et al. 2012), is of course of much interest. *eROSITA* will scan the X-ray sky at unprecedented flux levels, making it possible to recognise orphaned CCOs and M7-like neutron stars through their residual thermal emission, either among the known radio pulsar population or even if these elusive objects are intrinsically radio silent.

Acknowledgements. We thank the anonymous referee for useful comments and suggestions that helped to improve the paper. The work of A.M.P. is supported by the Deutsche Forschungsgemeinschaft (PI 983/1-1). R.T. is partially funded through an INAF PRIN grant. S.B.P. was supported by the Russian Science Foundation, project 14-12-00146. The authors acknowledge the use of the ATNF Pulsar Catalogue (Manchester et al. 2005, http://www.atnf.csiro.au/research/pulsar/psrcat), the McGill Online Magnetar Catalog (Olausen & Kaspi 2014, http://www.physics.mcgill.ca/~pulsar/magnetar/main.html), the RRATalog of discovered rotating radio transients (http://astro.phys.wvu.edu/rratalog), as well as the online catalogue of isolated neutron stars with significant thermal emission, described in Viganò et al. (2013, http://www.neutronstarcooling.info).

References

Agüeros, M. A., Posselt, B., Anderson, S. F., et al. 2011, AJ, 141, 176
Aguilera, D. N., Pons, J. A., & Miralles, J. A. 2008, ApJ, 673, L167
Arnaud, K. A. 1996, in Astronomical Data Analysis Software and Systems V, eds. G. H. Jacoby, & J. Barnes, ASP Conf. Ser., 101, 17
Belczynski, K., Lorimer, D. R., Ridley, J. P., & Curran, S. J. 2010, MNRAS, 407, 1245
Bignami, G. F., Caraveo, P. A., De Luca, A., & Mereghetti, S. 2003, Nature, 423, 725
Bogdanov, S. 2014, ApJ, 790, 94
Bogdanov, S., Grindlay, J. E., Heinke, C. O., et al. 2006, ApJ, 646, 1104
Bogdanov, S., van den Berg, M., Servillat, M., et al. 2011, ApJ, 730, 81
Bogdanov, S., Ng, C.-Y., & Kaspi, V. M. 2014, ApJ, 792, L36
Broos, P. S., Townsley, L. K., Feigelson, E. D., et al. 2011, ApJS, 194, 2
Buccheri, R., Bennett, K., Bignami, G. F., et al. 1983, A&A, 128, 245
Chevalier, R. A. 1989, ApJ, 346, 847
Chieregato, M., Campana, S., Treves, A., et al. 2005, A&A, 444, 69
de Luca, A. 2008, in 40 Years of Pulsars: Millisecond Pulsars, Magnetars and More, eds. C. Bassa, Z. Wang, A. Cumming, & V. M. Kaspi, AIP Conf. Ser., 983, 311
De Luca, A., Caraveo, P. A., Mereghetti, S., Negroni, M., & Bignami, G. F. 2005, ApJ, 623, 1051
Geppert, U., Page, D., & Zannias, T. 1999, A&A, 345, 847
Gotthelf, E. V., & Halpern, J. P. 2010, in BAAS, 42, 694
Gotthelf, E. V., Halpern, J. P., & Alford, J. 2013a, ApJ, 765, 58
Gotthelf, E. V., Halpern, J. P., Allen, B., & Knispel, B. 2013b, ApJ, 773, 141
Haberl, F. 2007, Ap&SS, 308, 181
Haberl, F., Motch, C., Zavlin, V. E., et al. 2004, A&A, 424, 635
Halpern, J. P., & Gotthelf, E. V. 2010, ApJ, 709, 436
Halpern, J. P., Bogdanov, S., & Gotthelf, E. V. 2013, ApJ, 778, 120
Harding, A. K. 2013, Frontiers of Physics, 8, 679
Ho, W. C. G., Potekhin, A. Y., & Chabrier, G. 2008, ApJS, 178, 102
Hobbs, G., Lorimer, D. R., Lyne, A. G., & Kramer, M. 2005, MNRAS, 360, 974
Jansen, F., Lumb, D., Altieri, B., et al. 2001, A&A, 365, L1
Kaminker, A. D., Potekhin, A. Y., Yakovlev, D. G., & Chabrier, G. 2009, MNRAS, 395, 2257
Kaplan, D. L. 2008, in 40 Years of Pulsars: Millisecond Pulsars, Magnetars and More, ed. C. Bassa, Z. Wang, A. Cumming, & V. M. Kaspi, AIP Conf. Ser., 983, 331
Kaplan, D. L., & van Kerkwijk, M. H. 2011, ApJ, 740, L30
Kaplan, D. L., Kamble, A., van Kerkwijk, M. H., & Ho, W. C. G. 2011, ApJ, 736, 117
Kargaltsev, O., Durant, M., Pavlov, G. G., & Garmire, G. 2012, ApJS, 201, 37
Kaspi, V. M. 2010, Proc. National Academy of Science, 107, 7147
Keane, E. F., & Kramer, M. 2008, MNRAS, 391, 2009
Klochkov, D., Suleimanov, V., Pühlhofer, G., et al. 2015, A&A, 573, A53
Lasker, B. M., Lattanzi, M. G., McLean, B. J., et al. 2008, AJ, 136, 735
Leutenegger, M. A., Kahn, S. M., & Ramsay, G. 2003, ApJ, 585, 1015
Luo, J., Ng, C.-Y., Ho, W. C. G., et al. 2015, ApJ, 808, 130
Manchester, R. N., Hobbs, G. B., Teoh, A., & Hobbs, M. 2005, AJ, 129, 1993
McLaughlin, M. A., Rea, N., Gaensler, B. M., et al. 2007, ApJ, 670, 1307
Mereghetti, S. 2008, A&ARv, 15, 225
Merloni, A., Predehl, P., Becker, W., et al. 2012, ArXiv e-prints [arXiv:1209.3114]
Mori, K., & Ho, W. C. G. 2007, MNRAS, 377, 905
Mori, K., Chonko, J. C., & Hailey, C. J. 2005, ApJ, 631, 1082
Ngoumou, J., Preibisch, T., Ratzka, T., & Burkert, A. 2013, ApJ, 769, 139
Olausen, S. A., & Kaspi, V. M. 2014, ApJS, 212, 6
Page, D., Prakash, M., Lattimer, J. M., & Steiner, A. W. 2011, Phys. Rev. Lett., 106, 081101
Pavlov, G. G., Shibanov, Y. A., Zavlin, V. E., & Meyer, R. D. 1995, in The Lives of the Neutron Stars, eds. M. A. Alpar, U. Kiziloglu, & J. van Paradijs, 71
Pavlov, G. G., Zavlin, V. E., & Trümper, J. 1999, ApJ, 511, L45
Pecaut, M. J., & Mamajek, E. E. 2013, ApJS, 208, 9
Pires, A. M., Motch, C., & Janot-Pacheco, E. 2009a, A&A, 504, 185
Pires, A. M., Motch, C., Turolla, R., Treves, A., & Popov, S. B. 2009b, A&A, 498, 233
Pires, A. M., Motch, C., Turolla, R., et al. 2012, A&A, 544, A17
Popov, S. B., Colpi, M., Prokhorov, M. E., Treves, A., & Turolla, R. 2003, A&A, 406, 111
Potekhin, A. Y., Chabrier, G., & Yakovlev, D. G. 1997, A&A, 323, 415
Predehl, P., Andritschke, R., Becker, W., et al. 2014, in SPIE Conf. Ser., 9144, 1
Rutledge, R. E., Fox, D. B., & Shevchuk, A. H. 2008, ApJ, 672, 1137
Sanwal, D., Pavlov, G. G., Zavlin, V. E., & Teter, M. A. 2002, ApJ, 574, L61
Skrutskie, M. F., Cutri, R. M., Stiening, R., et al. 2006, AJ, 131, 1163
Smith, N. 2006, ApJ, 644, 1151
Strüder, L., Briel, U., Dennerl, K., et al. 2001, A&A, 365, L18
Suleimanov, V. F., Klochkov, D., Pavlov, G. G., & Werner, K. 2014, ApJS, 210, 13
Swanepoel, J. W. H., de Beer, C. F., & Loots, H. 1996, ApJ, 467, 261
Tiengo, A., Esposito, P., Mereghetti, S., et al. 2013, Nature, 500, 312
Townsley, L. K., Broos, P. S., Chu, Y.-H., et al. 2011, ApJS, 194, 15
Turner, M. J. L., Abbey, A., Arnaud, M., et al. 2001, A&A, 365, L27
Turner, M. L., Rutledge, R. E., Letcavage, R., Shevchuk, A. S. H., & Fox, D. B. 2010, ApJ, 714, 1424
Turolla, R. 2009, in Astrophys. Space Sci. Lib. 357, ed. W. Becker, 141
Viganò, D., Pons, J. A., & Miralles, J. A. 2012, Comput. Phys. Comm., 183, 2042
Viganò, D., Rea, N., Pons, J. A., et al. 2013, MNRAS, 434, 123
Viganò, D., Perna, R., Rea, N., & Pons, J. A. 2014, MNRAS, 443, 31
Weisskopf, M. C., Tennant, A. F., Yakovlev, D. G., et al. 2011, ApJ, 743, 139
Wilms, J., Allen, A., & McCray, R. 2000, ApJ, 542, 914
Yakovlev, D. G., & Pethick, C. J. 2004, ARA&A, 42, 169
Yakovlev, D. G., Gnedin, O. Y., Kaminker, A. D., & Potekhin, A. Y. 2008, in 40 Years of Pulsars: Millisecond Pulsars, Magnetars and More, eds. C. Bassa, Z. Wang, A. Cumming, & V. M. Kaspi, AIP Conf. Ser., 983, 379
Yakovlev, D. G., Ho, W. C. G., Shternin, P. S., Heinke, C. O., & Potekhin, A. Y. 2011, MNRAS, 411, 1977
Zacharias, N., Monet, D. G., Levine, S. E., et al. 2004, in BAAS, 36, 1418
Zane, S., Haberl, F., Israel, G. L., et al. 2011, MNRAS, 410, 2428
Zavlin, V. E., Pavlov, G. G., & Shibanov, Y. A. 1996, A&A, 315, 141